1 Analyzing Particle Movements at Soil Interfaces

Hagen Spies, Oliver Beringer, Hermann Gröning, and Horst Haußecker

Interdisziplinäres Zentrum für Wissenschaftliches Rechnen (IWR)
Universität Heidelberg, Germany

1.1 Introduction 4
1.2 Previous investigations 4
1.3 Experimental setup 4
1.3.1 The pressure tank 5
1.3.2 Endoscopes 5
1.4 Image analysis 7
1.4.1 Correcting for inhomogeneous illumination 7
1.4.2 Motion detection 8
1.4.3 Motion compression 8
1.4.4 Optical flow estimation 9
1.4.5 Mixing parameters 12
1.4.6 Estimation of water flow 15
1.4.7 Image processing summary 15
1.5 Results 15
1.5.1 Movements due to pressure changes 15
1.5.2 Observed and predicted motion 17
1.5.3 Mixing 18
1.5.4 Flow in gravel 19
1.5.5 Results summary 19
1.6 Conclusions and future activities 20
1.7 References 21

1.1 Introduction

In order to protect utilizable floor space from rivers changing their course it has long been necessary to fortify embankments. The slope stability of embankment constructions is greatly influenced by pore water pressures induced by hydraulic load changes as a result of ship traffic. This influence was analyzed in laboratory measurements which are presented here. Air bubbles contained in the pore water greatly delay pressure transmission. Thus changing hydrodynamic load conditions may lead to locally and temporally acting excess pore water pressure and therefore to transient pore water flow. The transport of movable soil particles is strongly dependent on the acting hydraulic gradients in the water flow. This water flow may in turn cause destabilization of the soil structure. Under certain conditions even fluidization of soil layers occurs, resulting in the collapse of the embankment.

1.2 Previous investigations

Previous investigations focused on the pressure distribution within soil structures. From pressure gauges inserted at various locations it could be infered that pressure changes do not spread unhindered. From empirical investigations the following formula for the excess pore water pressure Δp depending on the depth h was derived [Köhler, 1993]:

$$\Delta p(h,t) = \rho_w \, \Delta h \, g \, (1 - a(t) \, e^{-b(t)h}) \; . \tag{1.1}$$

Where ρ_w is the density of water, Δh is the water level change and g the gravity acceleration. The two time dependent parameters $a(t)$ and $b(t)$ vary with the soil type and the acting hydraulic load. The pressure distribution is mainly governed by $b(t)[1/\mathrm{m}]$ which in turn depends on the permeability of the soil and the hydraulic gradient. However, no attempt has been made to study the processes on a microscopic scale. The following sections describe our approach to the task which is based on the analysis of images gathered with endoscopes.

At a previous stage of the project we focused on the detection of moving areas within the soil structure [Köhler et al., 1996; Gröning, 1996; Haußecker, 1993]. From those areas motion frequency can be deduced and compared to the amount of motion expected at the given pressure situation. These experiments showed promising results, thus we extended our image analysis towards a quantitative investigation of sediment motion.

1.3 Experimental setup

Experiments where carried out at a specifically build large pressure tank located at the Federal Waterways Engineering and Research Institute in Karlsruhe, Germany.

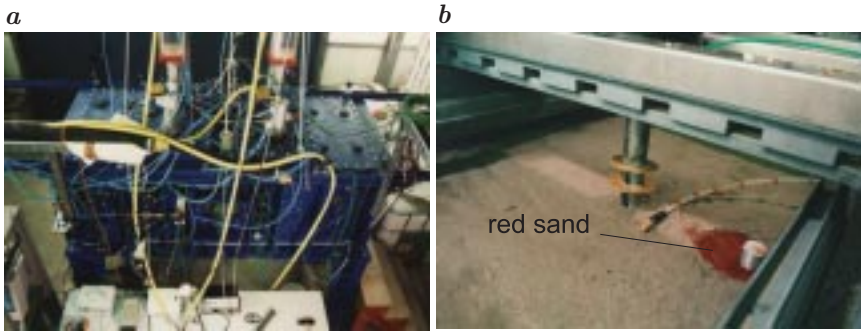

Figure 1.1: ***a*** *The pressure tank during measurements.* ***b*** *Mounting of endoscopes and pressure gauges.*

1.3.1 The pressure tank

The tank itself is roughly two meters long, 80 cm wide and 80 cm high. With this unique device it is possible to apply pressure gradients in all directions superimposed by steady and transient water flow in a pressure environment of up to three bar. Pressure loadings may act from above and underneath the soil structure simultaneously and the water can be forced to flow either above the sediment layers or directly through the sediment in separate depth layers. Several adjustable endoscope inlets allow to observe all critical areas within the sediment. Figure 1.1a shows the pressure tank during the summer 1997 measurement campaign.

During this campaign the tank was filled with Sand of a diameter range from 0.05 to 0.5 mm. On top of this main sediment body follows a 10 cm layer of gravel. This layer is again stabilized from above by a variable hydraulic pressure distributed via stell bars and metal sheets. This allows to simulate revetment or other load that is usually present to stabilize river embankments. It is one goal of our research to study how much additional load is needed to maintain a stable configuration.

At one location directly below the gravel two layers of red and green colored sand are placed. In Figure 1.1b the top of the red layer can be observed. One of the endoscopes is placed in such a way that the interface between the two color layers can be imaged. From these images it is then possible to obtain information about mixing in that area (see Sect. 1.4.5). The other endoscopes are placed directly at the gravel-sand interface. Additionally a flexible endoscope is used within the gravel layer to study the water flow within the pore volume.

1.3.2 Endoscopes

We use rigid *endoscopes* with a viewing direction of 90° and a diameter of 10 mm. An external cold light source coupled via a fiber light conductor

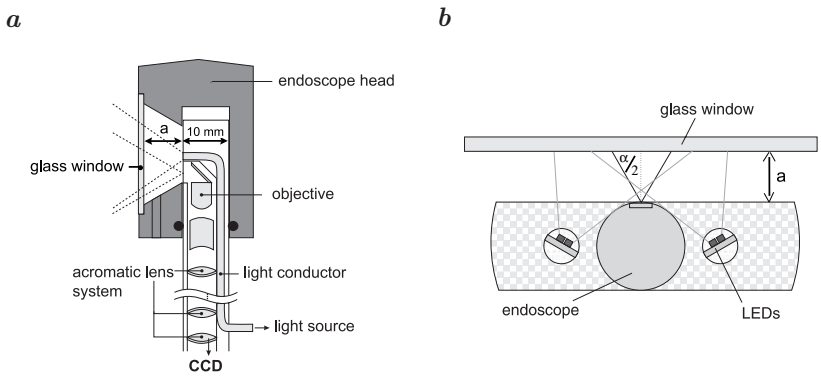

Figure 1.2: *Setup of the endoscope:* ***a*** *vertical cross section through the endoscope and* ***b*** *horizontal cross section with the new illumination setup using LED's.*

to the endoscope can be used for illumination (Fig. 1.2). With a viewing distance of $a = 8\,\text{mm}$ and an aperture angle $\alpha = 60°$ we obtain a viewing area of roughly 6 by 6 mm. An achromatic lens system allows to adjust magnification by a factor of up to 2. For exact geometric calibration we used a grid target. Cross sections through the endoscope and protection head are given in Figure 1.2a.

Homogeneous illumination using LED's. Using the fiber optic *illumination* integrated in the endoscope, specular reflexes on the glass window can't be avoided. These and the inhomogeneous illumination result in over- and underexposed regions which drastically reduces the quality of the acquired images. Hence a new setup has been devised with LED panels on both sides of the endoscopes. Thus the angle of incidence on the glass window is far smaller than with the fiber light conductor. Like this no reflexes occur in the viewing area. This setup is shown in Figure 1.2b. The improvement is illustrated in Figure 1.3a and b where a paper is placed on the glass window.

Flexible endoscope. The flexible endoscope consists of circularly arranged optic fibers. The resulting bundle has a diameter of 1.1 mm and length of 80 cm. For illumination a cold light source is coupled to a ring of fiber conductors. For utilization in the rough environment of the pressure tank the actual endoscope is surrounded by a protection cover, increasing the diameter to 1.4 mm. The end is covered by a 2 cm long steel tube with a glass window at the end. In order to introduce as little disturbance to the water current as possible, the endoscope is placed in a PVC sphere of similar size as the surrounding gravel stones to form a pore volume. Figure 1.4 shows the described setup. For visualization of the water flow

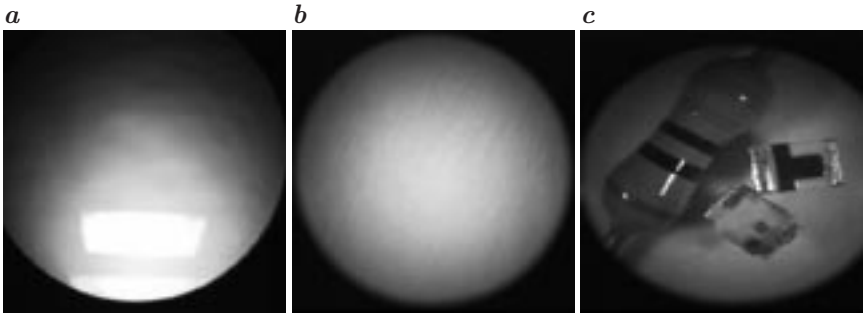

Figure 1.3: *Comparison of the new LED-based and old fiber illumination setup:* ***a*** *old setup,* ***b*** *and* ***c*** *new setup.*

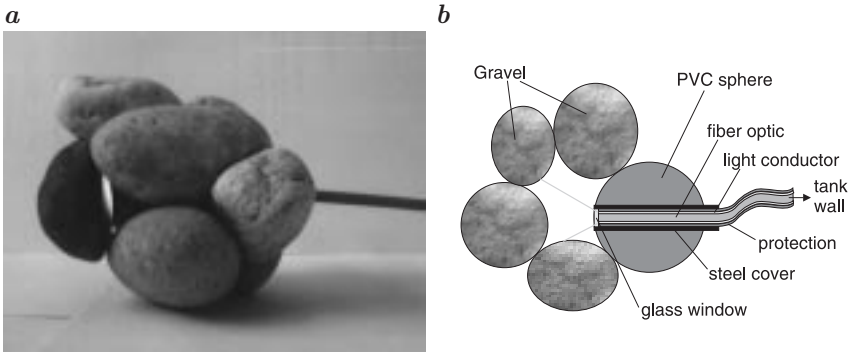

Figure 1.4: *The flexible endoscope:* ***a*** *placed in a gravel package and* ***b*** *cross section through the setup.*

latex particles are added. These particles possess nearly the same density as water, which makes them well suited for flow analysis.

1.4 Image analysis

1.4.1 Correcting for inhomogeneous illumination

Due to two different causes the collected imagery is brighter in the center:

- Firstly, when using the fiber optic light conductor the illumination is not homogeneous and often specular reflexes occur. With the new LED illumination setup as described in Section 1.3.2 these reflexes can be avoided and a far better illumination is achieved.
- The second effect is due to vignetting which results from the wide angle lens system integrated in the endoscope. Vignetting can not be avoided with the present setup and has to be corrected for. For correction we use a normalized highly smoothed image as correction factor. The result

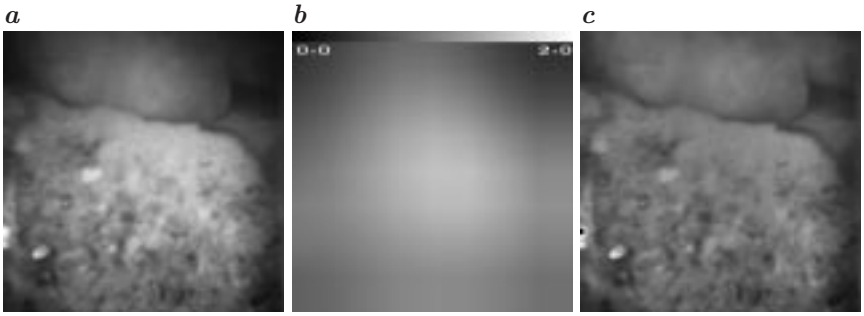

Figure 1.5: *Illumination correction:* ***a*** *example image,* ***b*** *smoothed image normalized to a mean of 1 and* ***c*** *corrected image.*

can be seen in Figure 1.5 were the 5th level of a Gaussian pyramid is used for smoothing of the example image.

1.4.2 Motion detection

In the first phase of the investigations grain movements were detected. Relating the amount of movement to the acting hydraulic loads gives insights into the conditions under which the soil structure becomes unstable. As a wide range from very slow to rapid motion is encountered a special motion detection algorithm is needed which is introduced next.

We do not intend to detect the complete area of the moving particles. It is only the boundaries of low textured objects that appear to move. Coding only these pixels provides enough information for reconstruction. Thus we use a simplified motion detection algorithm for compression purposes. For noise reduction and efficiency reasons we use the first level of a Gaussian pyramid. A special implementation of the Gaussian pyramid significantly reduces the number of computations [Haußecker et al., 1995]. Secondly a binomial smoothing operator is applied in the time direction. The resulting images show practically no noise and changing areas are easily detected using a threshold on the temporal derivative. This threshold is set rather low and outliers are removed by a subsequent morphological erosion.

1.4.3 Motion compression

The detection of moving areas within image sequences can be readily exploited for *image compression* purposes. The scenes under consideration often show long periods of little or no motion. Storing the complete images thus introduces a lot of redundancy. We typically investigate 800 images of size 512×512 pixels, resulting in approximately 205 MB of data. Using European video norm (PAL, 25 frames per second) this equates to 32 seconds of observation time. For colored images this number has to be halved again

as both red and green channels are used. During a measurement campaign large amounts of data quickly pile up. Lossless compression algorithms such as *LZW* or *ZIP* achieve reduction rates of approximately 20% on our data. In order to achieve better compression rates we used a lossy method described in this section.

The goal of the envisaged compression was not to be lossless with regard to grayvalue information but rather to keep the derived physical results unchanged. The fundamental image processing task considered here is the estimation of velocities. We therefore examined to which extend the calculation of optical flow is influenced by our compression technique.

For compression we proceed as follows: From the original image sequence we compute the moving areas, the remaining pixels are set to zero. The resulting image contains large black areas and is well suited for standard compression techniques. We achieved compression rates of more than 80%. Reconstruction is done by recursively using previously reconstructed pixels where no motion was detected, thus only one image is needed for the initialization of the reconstruction algorithm. Figure 1.6 shows a flow chart of the algorithm.

Figure 1.7 shows the first image of three generated test sequences that were used for evaluating the algorithm. In all three test cases the objects were fully detected for velocities exceeding 0.05 pixel/frame. Smaller velocities lead to only partially segmented objects. The graylevel difference between original and reconstructed image remains in average below two. For the test normal distributed noise with a standard deviation of 1.2 graylevels was added to the images, corresponding to the typical noise levels as found for our cameras.

As mentioned above the idea behind the compression was not to change the final velocity estimates. An investigation towards this end is presented in the next section.

1.4.4 Optical flow estimation

For velocity calculation of soil movements we use the structure tensor technique as described in, Vol. 2 Sect. **??**. As the image material used here is relatively low in contrast a low threshold on the trace of the Tensor has to be used. For the results described below we used only areas where the trace exceeded a value of 5. Furthermore there are areas that show very little spatial variation wich makes motion estimation difficult. The coherence measure provides a criterion to decide how reliable the optical flow computation was performed. With the given data it is necessary to use a rather low threshold of 0.5 on the coherence. Otherwise the displacement vector field becomes to sparse.

A survey on the achievable accuracy with the Tensor method under these circumstances showed a strong dependence on image content. Figure 1.8a shows the relative error in velocity estimation on the generated

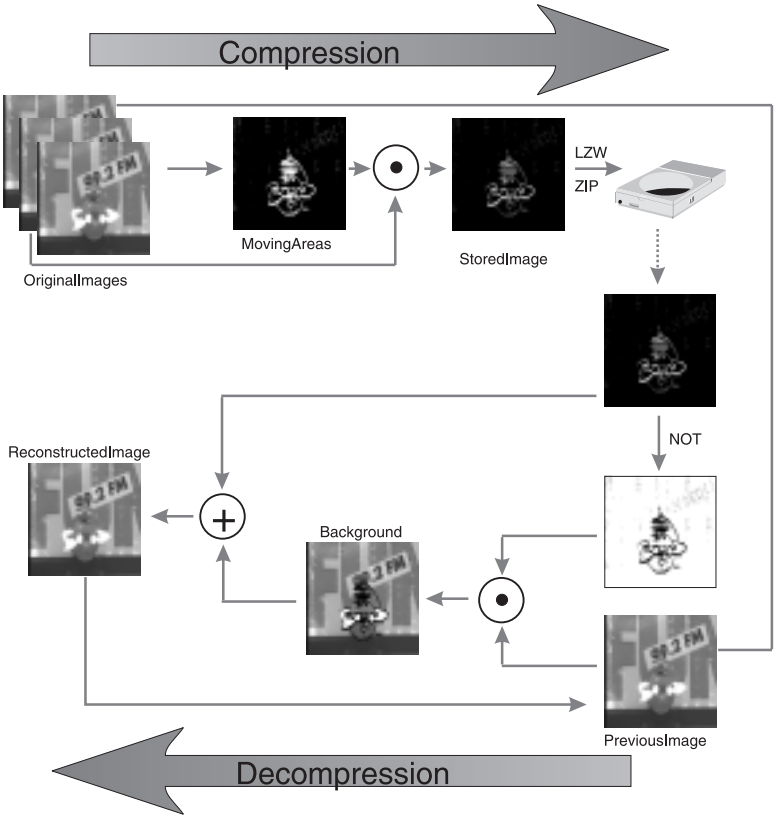

Figure 1.6: *The steps involved in the compression algorithm.*

test data of Fig. 1.7b and c with single and multiple gaussians. Due to the small object size aliasing effects deteriorate the achieved accuracy dramatically for velocities over 1 pixel/frame. Secondly those Gaussians pose a difficult problem also at small velocities because they contain large regions with very low contrast. Images of soil layers typically show more contrast, bigger objects and moderate velocities. For the typical velocity range encountered here (0.05 to 1 pixel/frame) we found that a relative error of 5% can be used as an upper margin.

Compression and optical flow calculation. As stated before, the main objective for our compression is not to hinder the accurate estimation of optical flow. We used the generated test data of Fig. 1.7b and c to investigate the influence of compression and decompression prior to the analysis with the structure tensor. As can be seen in Figure 1.8a the compression does not alter the performance. Figure 1.8b shows the computed opti-

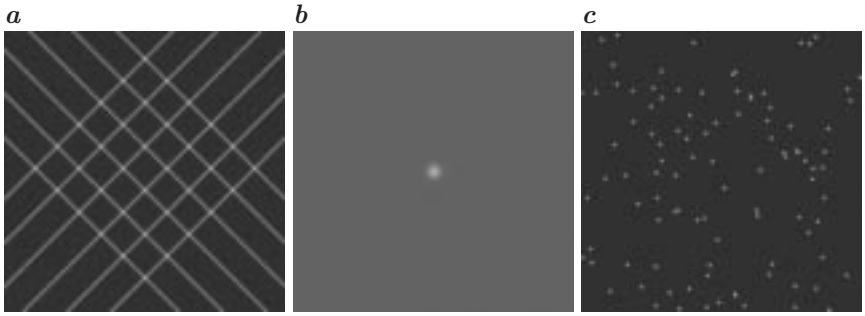

Figure 1.7: *One Frame of the generated test images used.* ***a*** *grid,* ***b*** *single gaussian ($\sigma = 5\,pixel$) and* ***c*** *multiple Gaussians ($\sigma = 1\,pixel$).*

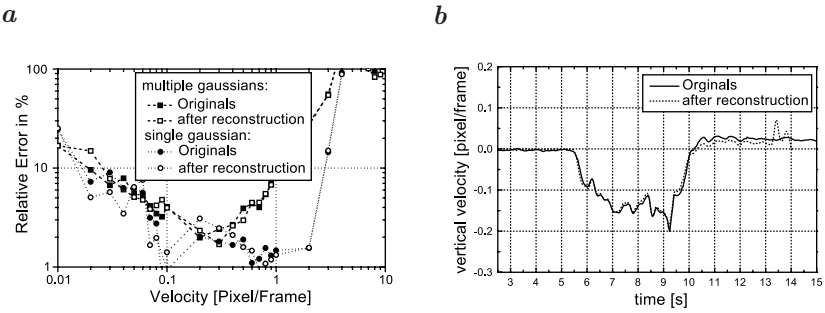

Figure 1.8: *Optical flow estimation with the structure Tensor technique on original images and on reconstructed images after compression:* ***a*** *relative error on generated test data and* ***b*** *calculated velocity on an image sequence of the sediment boundary layer.*

cal flow on an example sequence of the gravel-sand boundary. Again the compression doesn't alter the outcome.

Normalized convolution. As described above the computation of optical flow can only be performed accurately on the subset of the image where the coherence exceeds a certain threshold. Even though we use a low value the resulting displacement field is rather sparse (Fig. 1.9a). We assume the movement of the soil structure to be smooth due to frictional forces between particles. Then a dense velocity field can be interpolated from the sparse velocity data by means of the normalized convolution, Vol. 2 Chap. **??**. The coherence measure serves as our confidence measure, where we consider only the previously segmented areas. For effective computation we use the binomial smoothing operator in form of a Gaussian pyramid for averaging. Empirical test showed that the second pyramid level gives best results with respect to the trade-off between fill factor and over-smoothing. Figure 1.9a shows the calculated vertical velocity where the coherence measure exceeds

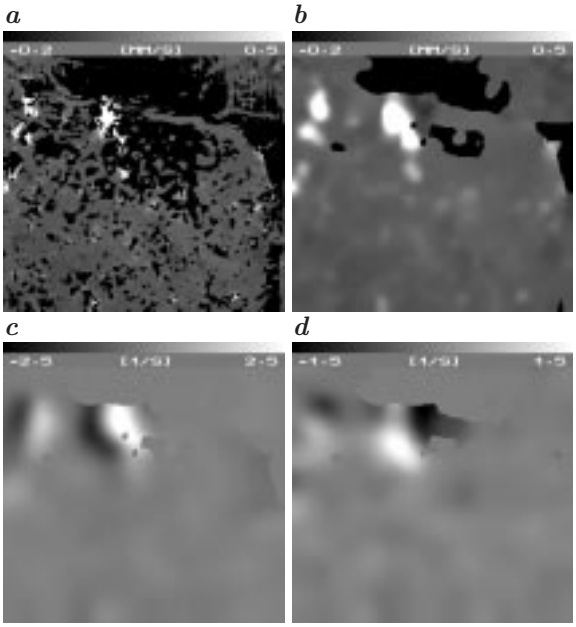

Figure 1.9: *Interpolation of a dense displacement vector field from a sparse field by normalized convolution and calculated characteristics of the velocity field:* ***a*** *sparse vertical velocity,* ***b*** *interpolated velocity,* ***c*** *value of the rotation and* ***d*** *divergence.*

0.5. Figure 1.9 b is the result after the convolution. There are still areas where no reliable velocity information can be obtained, because here the gaps are to wide to be filled.

1.4.5 Mixing parameters

To determine the amount of mixing, that occurs during a hydraulic load cycle, two different methods are utilized. One approach relies on the calculation of velocity field parameters such as divergence and rotation. Secondly a special experiment is carried out using color coded sand particles, which will be described in due course.

The rotation of a vector field is given by:

$$\mathrm{rot}(\boldsymbol{u}) = \nabla \times \boldsymbol{u} \ . \tag{1.2}$$

The resulting vector stands perpendicular to the image plane, its value characterizes the amount of circular movement, i.e. mixing. From the sign follows whether the movement occurs right- or leftcircular. Figure 1.9c shows an example of the calculated rotation value revealing a zone of strong circular motion directly at the soil gravel boundary. The relative expansion

of soil regions can also be parameterized by the divergence of the displacement vector field:

$$\mathrm{div}(\boldsymbol{u}) = \nabla \cdot \boldsymbol{u} \ . \tag{1.3}$$

Positive values indicate locally higher velocities than that of the surrounding material, negative values stand for comparatively lower velocities. Both cases lead to a change in the local soil structure.

Mixing from color coded particles. In order to study structural changes just below the gravel-sand boundary two areas of color coded sand were placed beneath the gravel. Via an endoscope a color camera images the border between a red and a green layer. At the beginning of a measuring campaign the two areas are divided by a clear cut line. This distinction gradually ceases to exist until both are nearly completely mixed, due to repetitive load changes. For a quantification of the mixing process it is first necessary to distinguish soil particles according to color.

We only use the red and green channels of an RGB-camera since only red and green sand has been used. The gain of the two channels are individually adjusted so that the two differently colored sand types show the same brightness.

In RG-space ideal colors are found on lines through the origin. Colored particles, on the other hand, are found to approximately follow a 2D gaussian distribution, because of statistical variations in their physical properties and orientation. From images where only one type of color is present, calculation of the normalized histogram $h(r, g)$ yields the according probability distributions. The normalized histograms for red, green and uncolored gray sediment are shown in Figure 1.10b. It is then possible to calculate the inertia Tensor:

$$\theta_{r,g} = \sum_{r,g} h(r, g)(\boldsymbol{x}^2 - \delta_{rg} rg) \ . \tag{1.4}$$

Eigenvector analysis of this symmetric Tensor yields the two principal axes $\boldsymbol{h}_0$ and $\boldsymbol{h}_1$. We define a new coordinate system were the origin is at the intersection of the two principal axes $\boldsymbol{h}_0^r$ and $\boldsymbol{h}_0^g$ to the lower eigenvalues. The eigenvector of the green distribution serves as one coordinate axis in this coordinate system as shown Figure 1.10a. In this new coordinate system we define a dividing line under an angle γ which is used for segmentation. This line is chosen so that there is equal fractional probability for the two distributions on opposing sides. This choice minimizes the amount of wrongly classified particles.

In the above we assume no gray sand to be present in the area under consideration, which can be validated by visual inspection. Problems occur if there are specular reflexes which show no color and come to lie close to the diagonal in RG-space. Such instances will be classified as green because the green distribution lies rather close to the diagonal, Figure 1.10b.

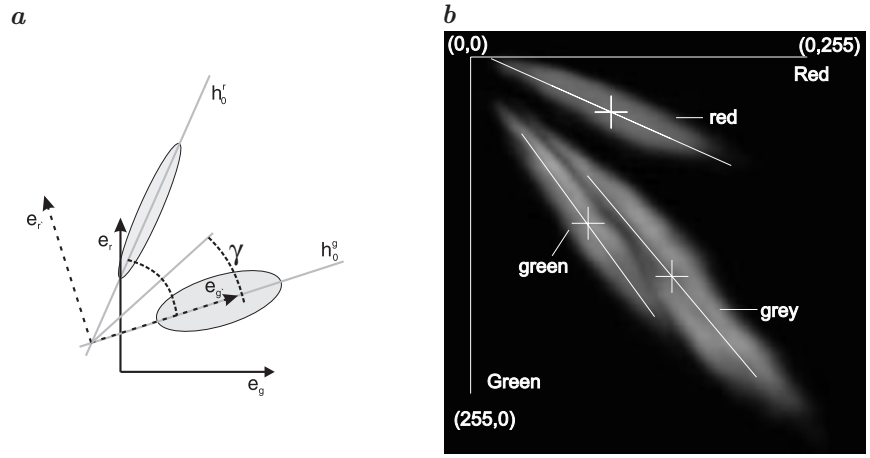

Figure 1.10: *Segmentation on color images:* ***a*** *coordinate transformation in RG-space and* ***b*** *example histograms with principal axes for red, green and gray (not colored) sand.*

If we describe the mixing of the layers as a diffusion process the particle concentrations $c_i(z,t),\ i \in \{r,g\}$ along the vertical z-axes follow the diffusion equation:

$$\frac{\partial c_i}{\partial t} = D\frac{\partial^2 c_i}{\partial z^2}, \tag{1.5}$$

where D is a diffusion constant. Initially we assume an ideal borderline to be located at position z_0. Thus we take $c(z < z_0, t = 0) = \text{const}$ and $c(z > z_0, t = 0) = 0$ as boundary conditions. Then equation Equation (1.5) is solved by the following function [Crank, 1975]:

$$c(z,t) = \frac{1}{2}\left(1 - \operatorname{erf}\left(\frac{z - z_0}{\sqrt{2}\,\|\sigma\|}\right)\right),\ \text{where } \sigma^2 = 2Dt\ . \tag{1.6}$$

Here erf denotes the error function, i.e. the integral over a Gaussian distribution. Fitting the measured vertical concentration of red/green particles at a given time to Equation (1.6) using a χ^2 fit, yields the two parameters z_0 and σ. From the first it is possible to deduce the movement of the complete sediment. Whereas the second does provide information about the width of the distribution, i.e. how far the layers have mixed.

At this point it has to be mentioned, that the described method is not very robust. This is mainly due to the fact that there are not enough particles (a sand grain is roughly 15 pixels in diameter) in the viewing area to provide sufficient statistics. However, this can be moderated in future experiments by enlarging the observed window.

1.4.6 Estimation of water flow

For the estimation of the water velocity field through the gravel cavities we use the established Particle Imaging Velocimetry (PIV) algorithm [Willert and Gharib, 1991]. Displacements between two frames are found by searching for the maximum value of their cross correlation, Vol. 2 Sect. **??**.

In order to study the trajectories of single particles we use a method known as Particle Tracking Velocimetry (PTV) [Hering et al., 1995], see Chap. **??**. With this approach, particles in one frame are located in the next frame and tracked over a series of images. However, due to the muddy water encountered in the tank it is not possible to segment many particles reliably. Thus we obtain only sparse velocity information with this method.

1.4.7 Image processing summary

Apart from the flow analysis presented in the previous section the image processing follows the same steps. The image sequences are compressed, using the algorithm described in Sect. 1.4.3, just after they were taken and then stored on CD's. After decompression, the images are first corrected for inhomogeneous illumination. Then the velocity fields are calculated using the structure tensor algorithm. From these fields it is already possible to obtain averaged velocities using only those areas where the coherence measure exceeds 0.5. However, for further calculations we need smooth and continuous fields. Those are obtained via the normalized convolution. As a last step rotation and divergence values are calculated to obtain mixing parameters. Figure 1.11 summarizes the image processing steps involved.

For the color images location z_0 and width σ of the boundary are calculated additionally as described in Section 1.4.5.

1.5 Results

Some exemplary results are shown in this section together with a simple model that allows an estimation of expected velocities at given pressure situations. For detailed results see [Beringer, 1998; Spies, 1998].

1.5.1 Movements due to pressure changes

We typically encounter a water draw down of 60 cm within 5 seconds after a passing ship in an inland channel corresponding to a pressure change 0f 60 mbar/s. Thus we sought to simulate this conditions under different situations. The most important parameter is the mechanical load placed upon the soil structure, which can simulated by additional hydraulic pressure from above. We studied three possibilities:

- No additional mechanical load: Only the weight of the steel bars and metal sheets, used to distribute the force, is present. This is far too little to prevent the soil from floating due to the entranced air content.

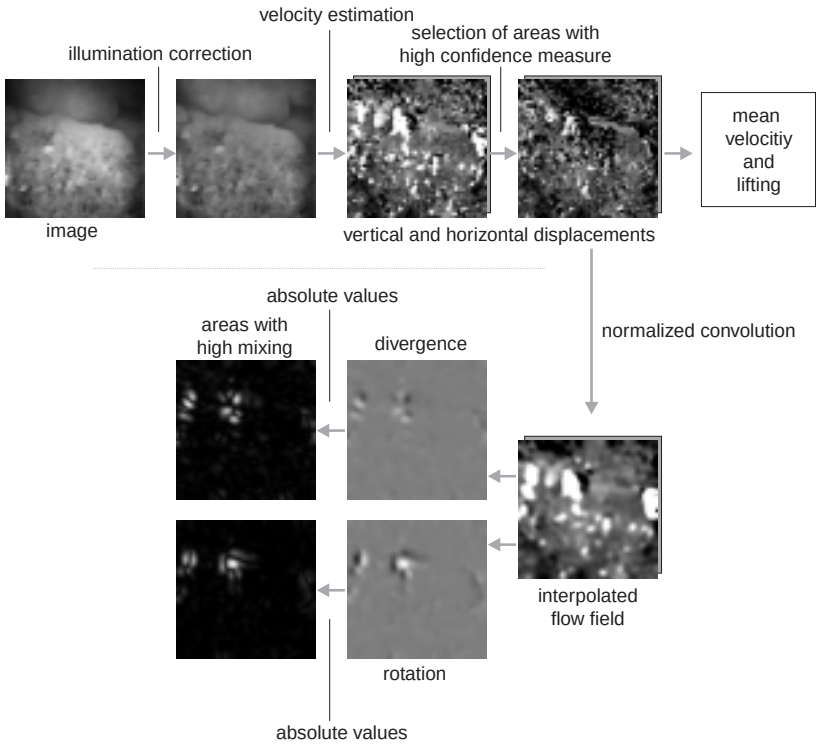

Figure 1.11: *Image processing summary.*

- Critical mechanical load: Enough pressure is used to stabilize the soil under normal conditions, i.e. pressure corresponding to four meters water level and a draw down as described above. However, already at lower water levels of 2 m destabilization sets in.
- Very high mechanical load: Under such a holding force the soil should remain stable even for higher draw down and low water levels.

As was said in the beginning, it is the air content in the soil that causes excess pore water pressure to build up. This pressure can in turn cause the sediment to flow like a fluid if there isn't enough mechanical load to stabilize.

Figure 1.12a shows the pressure measured by eight pressure gauges placed at different vertical positions above and in the sediment. Here their relative depth is already accounted for. In the beginning the system is in a stationary situation, after releasing the pressure it can clearly be seen how the pressure remains higher within the sediment for a certain time.

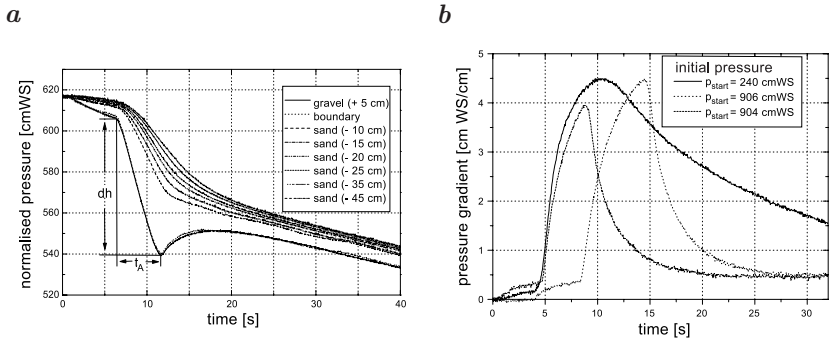

Figure 1.12: *Pressure curves* ***a*** *example draw down and* ***b*** *surface pressure gradient.*

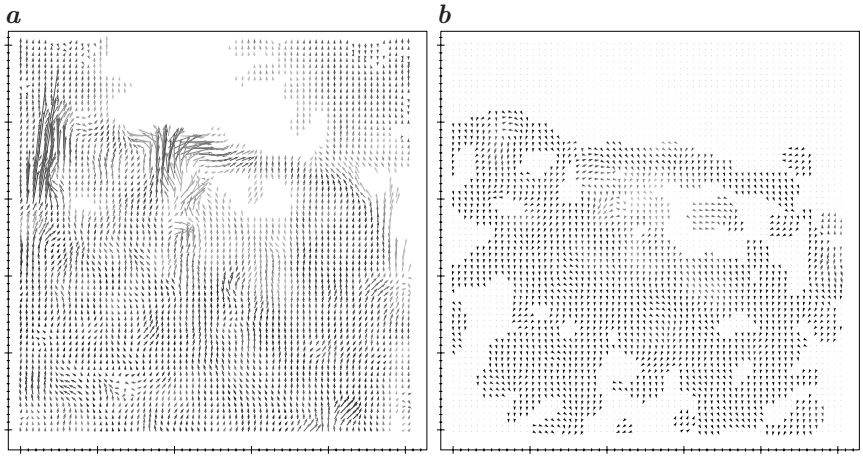

Figure 1.13: *Displacement vector fields:* ***a*** *just after the draw down and* ***b*** *20 seconds later.*

This leads to a pressure gradient acting at the interface which is plotted for some examples in Figure 1.12b.

The pressure gradient can cause the complete sediment to lift as can be seen from the displacement vector fields calculated with the structure tensor shown in Figure 1.13. In this example no additional mechanical load was placed on the sediment. The second velocity field corresponds to a later time where the movement is in the opposite direction as the excess pressure diminishes and the sediment settles down.

1.5.2 Observed and predicted motion

The described lifting will always occur to a certain extend as the air bubbles contained in the sediment expand, see Figure 1.14. If this expansion

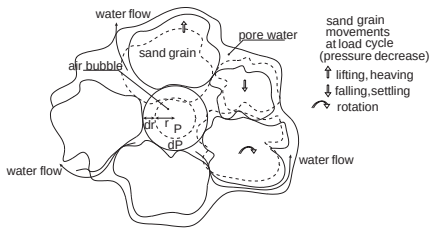

Figure 1.14: *Possible grain movements due to changing hydraulic load conditions.*

is the only cause of motion we can derive a simple model to quantify the accompanying movements. If, on the other hand, the water flow due to expanding air bubbles causes sediment particles to be drawn away this simple description will cease to appropriately explain the encountered motion.

For the relation between pressure P within the bubble (which equals the pressure of the surrounding liquid) and its volume V we take the ideal gas equation:

$$PV = \nu RT = \text{const} = c \ . \tag{1.7}$$

For constant temperature T a Taylor expansion of the volume for an infinitesimal pressure change dP and resubstitution of the bubble radius the following formula for the expected velocity can be derived, [Spies, 1998]:

$$u(t) = \frac{\mathrm{d}r(t)}{\mathrm{d}t} = -(\frac{c}{36\pi})^{\frac{1}{3}} \ P^{-\frac{4}{3}} \ \frac{\mathrm{d}P(t)}{\mathrm{d}t} \ . \tag{1.8}$$

If the expansion of the air bubbles is the only cause of motion, (1.8) should qualitatively describe the measured velocities. The free parameter c stems from the unknown air content and should remain constant with time.

In Fig. 1.15 the measured mean velocity and the expected velocity are plotted together. In the stable environment the model agrees surprisingly well with the measured data. For the other example, Figure 1.15b, the layers do not remain stable and the model doesn't capture the situation any more. However, the onset of the motion is still described correctly. This strongly suggests that the expansion of air in the sediment is the actual cause of motion.

1.5.3 Mixing

As described in section Section 1.4.5 we use divergence and rotation of the velocity field in order to quantify the amount of mixing. It turns out that both values are strongly related. This is not altogether surprising due to the inhomogeneous structure of the sediment. Wherever there are local velocity gradients they will lead to some circular movement. We obtain the

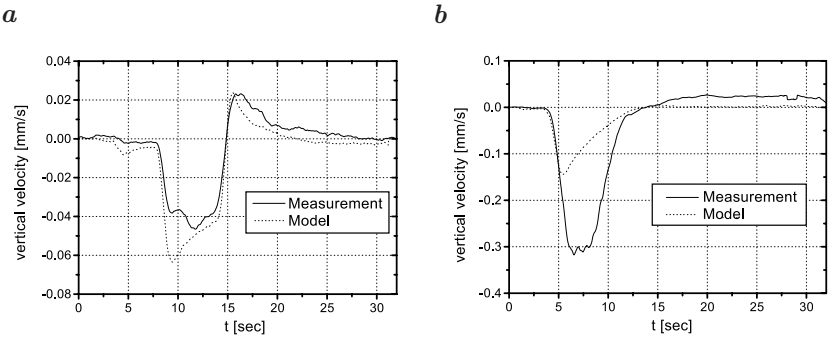

Figure 1.15: *Measured and calculated velocities:* ***a*** *stable setup and* ***b*** *unstable situation. Please note the different scales.*

expected results that the mean values are about one order of magnitude higher for experiments with lower mechanical load and lower water levels.

Color: An example Fit of the measured color distribution to Equation (1.6) is shown in Figure 1.16a. The first parameter extracted is the position of the red-green boundary z_0. This also describes the lifting of the complete sediment and can be compared with the result obtained from the integration of the velocities calculated with the structure tensor. Figure 1.16b compares these two approaches, they qualitatively yield the same values.

However, the above mentioned problem due to relatively bad statistics results in scattered and not very accurate results. Thus the computed boundary width σ only allows qualitative statements. One observation is that the width does increase by a factor of 2 over the whole measurement campaign. Secondly it is observed that within one experiment (one water level draw down) σ remains the same for stable situations and shows some broadening for unstable situations. Thus the broadening described by $\sigma(t)$ is a function of the numbers of draw-downs, rather than a function of t within one pressure change.

1.5.4 Flow in gravel

One example of the flow field within a pore volume is illustrated in Fig. 1.17a. This was calculated at a specific time step using PIV. From Figure 1.17b the trajectories of some particles, as computed with the PTV algorithm, over a time of 10 seconds can be seen.

1.5.5 Results summary

For high loads it is possible to account for sediment movements through the expansion of air bubbles within the soil. Here a simple model yields qualitatively good results. For lower loads a fundamentally different situation

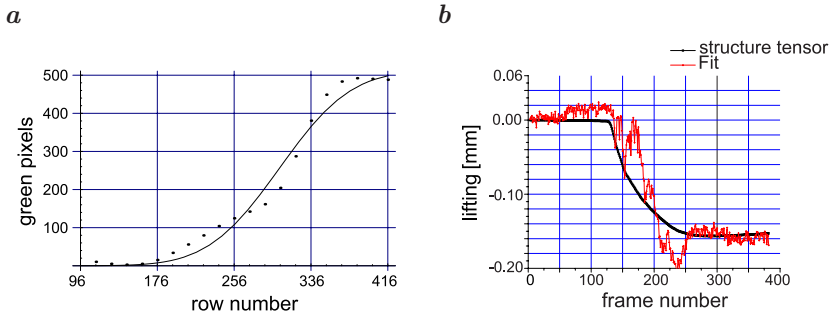

Figure 1.16: *Fitting the color distributions:* ***a*** *example fit and* ***b*** *comparison of computed lifting for the Tensor method and the fit.*

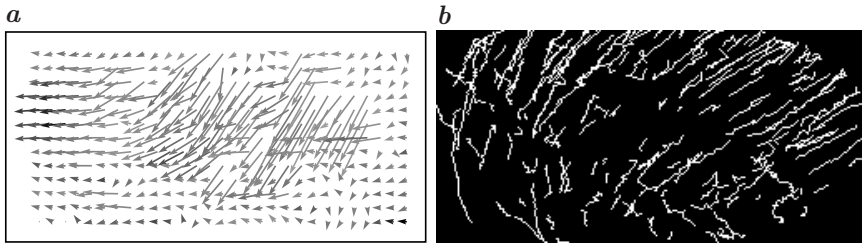

Figure 1.17: *Water flow in Gravel:* ***a*** *Eulerian motion vector field at one point in time and* ***b*** *Lagrangian trajectories for a sequence.*

appears. Velocities are higher by one order of magnitude (see also Fig. 1.15) and the model doesn't correspond to the measured displacements. The calculated mixing parameters show a similar picture, with much higher values for low load conditions. Image sequences taken under such circumstances clearly show a flow of sediment. This flow of material also becomes evident in the overall lifting of the sediment which is far greater ($> 2\,\mathrm{mm}$) for such unstable situations than it is for stable configurations ($0.01 \ldots 0.1\,\mathrm{mm}$).

1.6 Conclusions and future activities

A novel approach to investigate movements that occur at the boundary of gravel and sediment layers in river sediments was presented. To handle large data sets we introduced an image sequence compression scheme based on motion detection. It was shown that this compression doesn't alter the calculation of optical flow fields, computed with the structure tensor using the compressed image sequences. A fast method for color segmentation was presented. From the extracted distributions conclusions about lifting and mixing within sand layers can be derived.

A combined analysis of the captured velocities and the simultaneously measured pressure values reveals excess pore water pressure to be responsible for soil movements.

We also showed an approach to study water flow within a pore volume. The feasibility of this method could be demonstrated. In the near future systematic studies of horizontal flow fields in and above gravel layers are planned.

Acknowledgements. We would like to thank Mr. H.-J. Köhler from the Federal Waterways Engineering and Research Institute (BAW), Karlsruhe, for the support, both practical and financial, that made this project feasible.

1.7 References

O. Beringer. Ein meßsystem zur untersuchung von sedimentverlagerungen und durchmischungsprozessen mittels digitaler bildfolgenanalyse. Master's thesis, University of Heidelberg, 1998. 15

J. Crank. *The Mathematics of Diffusion.* Oxford University Press, New York, 1975. 14

H. Gröning. Mehrgitterbewegungssegmentierung und messungen am großen simulationstank zur bestimmung von sedimentverlagerungen. Master's thesis, University of Heidelberg, 1996. 4

H. Haußecker. Mehrgitter-bewegungssegmentierung in bildfolgen mit anwendung zur detektion von sedimentverlagerungen. Master's thesis, University of Heidelberg, 1993. 4

H. Haußecker, B. Jähne, and H. J. Köhler. Effektive filterverfahren auf mehrgitter-datenstrukturen. In *4. Symposium Bildverarbeitung '95*, Ostfildern, 29.11.-01.12. 1995. Technische Akademie Esslingen. 8

F. Hering, M. Merle, D. Wierzimok, and B. Jähne. A robust technique for tracking particles over long image sequences. In *ISPRS Intercommision Workshop 'From Pixels to Sequences'*, Zürich, 1995. 15

H. J. Köhler. The influence of hydraulic head and hydraulic gradient on the filtration process. In Brauns, Heibaum, and Schuler, editors, *Filters in Geotechnical and Hydraulic Engineering*, Rotterdam, 1993. Balkema. 4

H. J. Köhler, H. Haußecker, and B. Jähne. Detection of particle movements at soil interfaces due to changing hydraulic load conditions, localised by a digital image processing technique. In *2nd International Conference on Geofilters*, Montreal, May 1996. 4

H. Spies. Bewegungsdetektion und geschwindigkeitsanalyse zur untersuchung von sedimentverlaerungen und porenströmungen. Master's thesis, University of Heidelberg, 1998. 15, 18

C. E. Willert and M. Gharib. Digital particle image velocimetry. *Experiments in Fluids*, 10:181–193, 1991. 15